UC Irvine
UC Irvine Previously Published Works

Title

Garnet Electrolyte Surface Degradation and Recovery

Permalink

Journal

ISSN

Authors

Cheng, Lei
Liu, Miao
Mehta, Apurva
et al.

Publication Date

DOI

Peer reviewed

Garnet Electrolyte Surface Degradation and Recovery

Lei Cheng,[1,4,*] Miao Liu,[1] Apurva Mehta,[2] Huolin Xin,[3] Feng Lin,[1,†] Kristin Persson,[1,4] Guoying Chen,[1] Ethan J. Crumlin[5] and Marca Doeff [1,*]

1) Energy Storage and Distributed Resources Division, Lawrence Berkeley National Laboratory, 1 Cyclotron Road, Berkeley CA 94720 USA

2) Stanford Synchrotron Radiation Lightsource, SLAC National Accelerator Laboratory, Menlo Park, California 94025, USA.

3) Center for Functional nanomaterials, Brookhaven National Laboratory, Upton, NY 11973

4) Materials Sciences and Engineering Department, University of California at Berkeley, Berkeley, CA 94720 USA

5) Advanced Light Source, Lawrence Berkeley National Laboratory, 1 Cyclotron Road, Berkeley CA 94720 USA

† Current address: Department of Chemistry, Virginia Tech, Blacksburg, VA 24061, USA

Keywords: solid state battery, solid electrolyte, interface, surface engineering, interface recovery

*corresponding author: leicheng@lbl.gov; mmdoeff@lbl.gov

Abstract

Ceramic materials based on the garnet structure $Li_7La_3Zr_2O_{12}$ (LLZO) show great promise as lithium-ion conducting electrolytes for solid-state lithium batteries. However, these materials exhibit surface degradation when exposed to air and moisture, which adversely impacts their functioning in operating devices. In this work, we use several depth-profiling and *in situ* techniques to probe the nature of the surface reactions that occur when aluminum (Al)-substituted LLZO is exposed to air. These experiments show that a proton exchange reaction occurs near the surface of the LLZO and leads to change in its chemistry and structure, concomitant with the formation of Li_2CO_3. But these reactions can be readily reversed by heating samples at 250°C under an inert atmosphere to recover LLZO surface chemistry and structure. Symmetrical cells containing samples treated this way exhibited much lower area specific impedances than those containing air-exposed LLZO without the treatment, confirming the reversal of the degradation process. Our results show a process to rejuvenate LLZO surface and this opens the possibility of integrating this material in solid-state devices.

Introduction

Lithium ion battery technology has been a tremendous success, empowering the mobility and connectivity of human society. As the key component, the battery system is the very central technology for powering electric vehicles, mobile devices, wearable electronics, etc. In the last two decades, there has been significant progress in increasing energy density and lowering manufacturing cost. Yet current technology is unlikely to be sufficient to meet the requirements of next generation electric mobility.[1] Thus, developing the next generation of affordable, efficient, and high-energy devices is a grand challenge. The most attractive contender to meet this challenge is an all solid-state battery, which utilizes a high capacity lithium metal as an anode and has distinct safety advantages over lithium ion batteries in that no flammable liquid component is used in the device. [2,3]

A key component of the solid-state battery is a solid electrolyte that conducts lithium ions but not electrons. Ideally, it should have good ionic conductivity and reasonable chemical and mechanical stability under operating conditions, particularly at interfaces. The battery community has long acknowledged the various challenges of solid electrolytes associated with lithium anode or cathode/solid electrolyte interfaces, but understanding has been limited. To address this, simulation work has shed light from a thermodynamic perspective.[4-6] Although advanced synchrotron and neutron techniques have been tremendously helpful elucidating the material evolution *in situ* and *operando*, most of these were limited to electrode

materials for lithium ion batteries but not solid electrolytes.[7] In fact, direct experimental observation of chemical or/and electrochemical reactions at solid electrolyte interfaces/surfaces remains difficult, due partly to limitations of any single surface sensitive technique to directly observe interfaces, and challenges in resolving surface vs. bulk phenomena and correlating these to the electrochemical properties.

It is therefore necessary to experimentally study and elucidate reactions at interfaces by probing both the surface structure and the chemistry of the solid electrolyte interfacing the electrode components. Some progress has been made in recent years; for example, Janek and co-workers developed an X-ray photoelectron spectroscopy (XPS) methodology to study the surface reactivity of an LAGP (lithium aluminum germanium phosphate) type solid electrolyte with lithium metal *ex situ*.[8] Hirotoshi *et al.* used X-ray diffraction and XPS to reveal the Ohara® Glass solid electrolyte's local structure and composition change as a function of depth.[9] Recently, garnets related to $Li_7La_3Zr_2O_{12}$ (LLZO) have emerged as promising candidates for use as solid electrolytes, due to their high room temperature ionic conductivities, which range from 10^{-3} to 10^{-4} S/cm and their relatively good chemical stability. [10-12] Recent work has also has shown that the observed high interfacial impedance with lithium electrodes can be mitigated; e.g., Cheng et al. showed that the resistive interface is due to a thin Li_2CO_3 layer formed as a result of exposure of LLZO to CO_2 and H_2O in air, and that

removing Li_2CO_3 by polishing reduced the interfacial impedance substantially.[13,14] This chemical instability was further studied by Sanjuan and coworkers using Raman spectroscopy and X-ray and neutron powder diffraction.[15,16] Thermal annealing has been reported to improve interfacial resistance and Li cycling performance of garnets.[17] Sakamoto and co-workers used EIS and XPS to correlate the improved interfacial properties to the surface layer removal by polishing and annealing steps; the best performance was achieved from wet polishing and 500ºC annealing. [18,19] It is now understood that during exposure to moist air, LLZO undergoes exchange of lithium ions for protons, forming LiOH, which then reacts with CO_2 from the atmosphere to form Li_2CO_3. It is also possible, thermodynamically, for CO_2 to react directly with LLZO to produce Li_2CO_3 as indicated by first principles calculations, although this reaction is predicted to take place more slowly. [20-24] The formation of LiOH and Li_2CO_3 result in Li loss and proton uptake in the LLZO solid electrolyte near the surface. Details of the sub-Li_2CO_3 surface chemistry and its related structural evolution when LLZO degrades is yet unknown. Thus, developing *in situ* probes to capture both structural and chemical evolution of the LLZO sub-surface is of great significance both for the fundamental understanding of LLZO and for reliable processing to ensure good interfacial properties.

With these goals in mind, we combined ambient pressure X-ray photoelectron spectroscopy (APXPS), grazing incidence X-ray diffraction (GI-

XRD) and grazing incidence X-ray absorption spectroscopy (GI-XAS) to provide a detailed picture of the LLZO sub surface chemistry, crystal, and local structure evolution as LLZO is exposed to air and then heated under inert atmosphere, *in-situ*. The results demonstrate that treating LLZO at relatively low temperatures, can reverse the surface degradation caused by exposure to air, resulting in lowered interfacial impedance. This has significant positive implications for the processing of this material for use in practical solid-state devices.

Experimental

Aluminum (Al)-substituted LLZO pristine powders were prepared using a solid-state reaction as reported in our previous work,[14] using the following precursors: Li_2CO_3 (CAS# 554-13-2 Aldrich >99.0%), Al_2O_3 (Alcoa), ZrO_2 (CAS# 1314-23-4 Aldrich 99%) and $La(OH)_3$ (CAS# 14507-19-8 Alfa 99.95% REO). The as-prepared fresh powder was ground and then attrition milled at 450 RPM for 2 h with 2 mm diameter ZrO_2 media in isopropyl alcohol (IPA). The attrition-milled powder was used as-is to produce large-grained samples, as described in our previous work. [14] Cold uniaxial pressing using both 3/8 and 1 inch stainless dyes without any binder was utilized to produce pellets for study. Compacted LLZO pellets were sintered at 1100ºC for 12 h. The 3/8 inch size pellets were used for XPS, and 1 inch pellets were used for grazing incident XRD and EXAFS studies to accommodate larger X-ray footprints, especially at shallow angles. Sintered and densified LLZO was polished in air

progressively using polishing paper with grit number from 320-1000 dry. The 1 inch size LLZO pellets used in the GI-XRD and GI-XAS (extended X-ray absorption fine structure) measurements were further polished on a polishing cloth with 1 um diamond media dispersed in glycol to obtain sufficiently flat surfaces for study. The polishing was carried out in ambient environment until a shiny surface finish was achieved and the last step involved a brief DI-water cleaning of the finished surface. After the polishing procedure, some of the pellets were further exposed to air for a week before measurements.

Scanning electron micrographs (SEM) were obtained on samples, using a HITACHI TM-1000 tabletop microscope in secondary electron imaging (SEI) mode. The STEM image was acquired using an Hitachi 2700C dedicated scanning transmission electron microscopy equipped with a cold field emitter and a probe corrector.

The Grazing Incident X-Ray Diffraction (GI-XRD) experiments were performed at beamline 2-1 at Stanford Synchrotron Radiation Lightsource (SSRL). The specimen was mounted in a domed heating/cooling stage from Anton Paar. A polyether ether ketone (PEEK) dome was used for high X-ray transparency. Samples were either measured at room temperature or at various temperatures during the heating and cooling cycle, under helium gas flow sufficient to avoid exposure to air or moisture during the measurements. 1 mRad Soller Slits in front of a Vortex detector were used for low resolution

scans and a Si111 analyzer with a photomultiplier tube was used for high-resolution X-ray diffraction measurements in parallel-beam geometry. Pellets were scanned at various grazing angles with 8 keV X-rays. This X-ray energy was chosen for ease of comparison with laboratory XRD with a Cu Kα source.

The grazing incident X-ray absorption spectroscopy (GI-XAS) was performed at SSRL beamline 11-2. We used a 50 micron collimated beam in a vertically scattering grazing incidence geometry to limit the X-ray penetration depth to the near surface region. The fluorescence data was collected using a 100-element Ge detector (Canberra) at 90 degrees from the incidence beam in the horizontal plane. LLZO powder Zr X-ray absorption spectroscopy (XAS) experiments were conducted at SSRL beamline BL 4-1 in transmission mode using a Si (220) double crystal monochromator. Edge calibration was performed using Zr (17,988 eV) located in front of a reference ion-chamber and measured simultaneously with each spectral sample. All data processing, including normalization was carried out using the software SIXPACK by fitting a linear polynomial to the pre-edge region and a quadratic polynomial to the post-edge region of the absorption spectrum. The energy threshold, E_0 of the reference Zr foil was determined from the peak in the first derivative of the spectrum, and all spectra were linearly calibrated using the difference between the obtained E_0 and the tabulated absorption edge energy for metal K-edge. Pre-edge background subtraction and normalization were carried out. Background removal and

edge-step normalization were performed using the Athena module in the Demeter program pack. [25]

Ambient Pressure X-ray photoelectron spectroscopy (APXPS) was carried out at bending magnet beamline 9.3.2 of the Advanced Light Source (ALS) at Lawrence Berkeley National Laboratory (LBNL).[26] XPS data of Li 1s, C 1s, O 1s, Zr 3d and La 4d were collected at 640 eV from the top surface of LLZO samples in ultrahigh vacuum with a sampling size 1 mm in diameter. Binding energy correction of spectra was done by calibration to the C 1s photoemission peak of adventitious hydrocarbons at 284.8 eV.

AC impedance measurements were obtained on the dense pellets using a VMP3 multichannel potentiostat/galvanostat (Bio-Logic Science Instruments) equipped with frequency response analyzers. Typical dimensions of the pellets for EIS measurements were around 1.1 mm thick and 7.8 mm in diameter. Soft metallic lithium was first spread on both sides of the dense pellet. Afterwards, the pellet was assembled in a Swagelok-type cell between lithium foil disks on both sides. Physical contacts were maintained by compression of the spring at controlled displacement in the Swagelok cell with an estimated pressure of 200 kPa, derived from considering the spring displacement and spring constant. Samples were assembled in the same Swagelok cell with controlled displacement so that similar pressures were used for each. Impedance data were collected at frequencies from 1 MHz to 1 Hz.

Simulation

We employed density functional theory (DFT) calculations to investigate the structure variation in the LLZO system.[27] The Vienna ab initio software package (VASP)[28] was employed and the projector augmented-wave (PAW)[29] method was used to describe the wave functions near the core and the generalized gradient approximation (GGA) within the Perdew–Burke–Ernzerhof (PBE) parameterization was employed as the electron exchange–correlation functional.[30] The supercell consisted of $(Li_7La_3Zr_2O_{12})_8$, 192 atoms in total, hence, the Brillouin zone sampling of $1 \times 1 \times 1$ was adopted to ensure acceptable accuracy (using a k-point mesh of 500/number of atoms can reach the error of 5meV/atom for total energy for most compounds as tested by the Materials Project).[31] To evaluate the proton-Li+ ion exchange and its effect on the local structure, we evaluated $H_4Li_{52}La_{24}Zr_{16}O_{96}$ and $H_7Li_{49}La_{24}Zr_{16}O_{96}$, and we used ab initio molecular dynamics (AIMD) to extract the local structure at room temperature (300K). We allowed the system to relax to equilibrium and then ran the simulation for ~1500 steps. The obtained atomistic positions were then analyzed. Our quantitative calculation result on bond length is concluded from statistical analysis over large amount of samplings. Considering that the XAFS experimental observation is also an averaging result (over the measured volume, time), the simulation represents similar trends.

Results and Discussion

Figure 1 shows an SEM image of an LLZO pellet after the polishing procedure, which culminated with a final polishing step using 1 μm diamond media dispersed in glycol. The image shows a relatively flat surface with low roughness. Isolated porosity could be seen within the large grains (grain size 100-150 µm), likely a result of trapped air by fast grain growth. The typical isolated pore size is sub-micron in diameter. The density of a typical pellet is about 92% of the theoretical value.
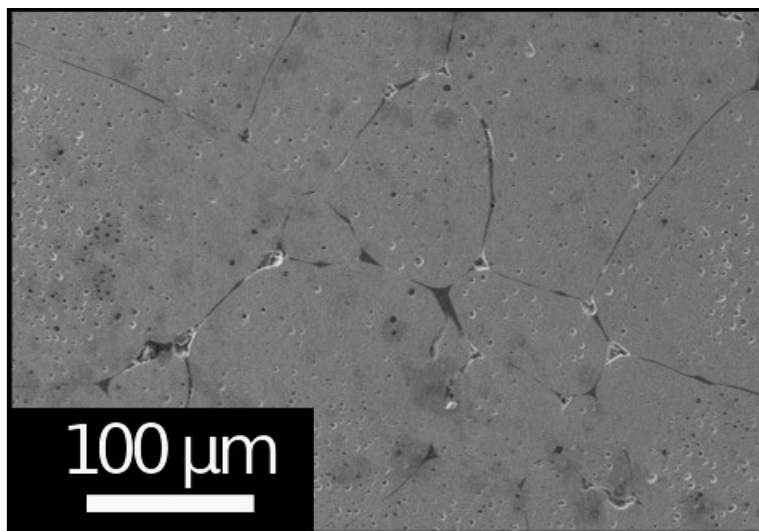
Figure 1. Top view SEM image of a polished garnet pellet

Figure 2 shows low resolution GIXRD patterns obtained on a polished pellet after exposure to air for a week. Based on the photon energy, and the

chemistry of LLZO and its density, the X-ray attenuation lengths at various grazing angles were estimated to be 3 nm, 20 nm, and 120 nm. The estimation was based on flat surface and should be only used for qualitative comparison. It is also noted here that, at these shallow angles, the X-ray beam footprint was on the order of mm^2, much larger than the grain size in the LLZO specimen. Thus the spectra obtained are on a polycrystalline material with randomly oriented crystals, similar to a powder XRD pattern obtained in a laboratory, except that the penetration depth is much less. Figure 2 also shows a powder XRD pattern obtained on LLZO, and a reference pattern calculated based on reference [32]. At all three grazing angles, a peak at approximately $2\theta=22^{\circ}$ attributable to Li_2CO_3 was clearly visible, although this was not seen in the powder pattern. Furthermore, the intensity of the Li_2CO_3 peak decreased as the angle was increased (probing depth increased). Peaks attributable to minor impurities phases (marked with an asterisk in Figure 2) were also observed in the GIXRD patterns. Similar impurities were observed on the surfaces of unpolished pellets using laboratory powder XRD. [14] Another difference between the powder XRD pattern and the GIXRD patterns is that the peaks attributable to LLZO are broader for the latter, particularly in the patterns collected at shallower angles, although no difference is seen in the breadth of the Li_2CO_3 peaks. For this reason, this is not likely to be an issue of degree of specimen flatness. It is more likely that the broadening of the LLZO peaks arises from disorder caused by strain gradient and reduced crystallinity, such as that which may

result from LLZO lattice contraction due to proton incorporation and loss of lithium close to the surface.
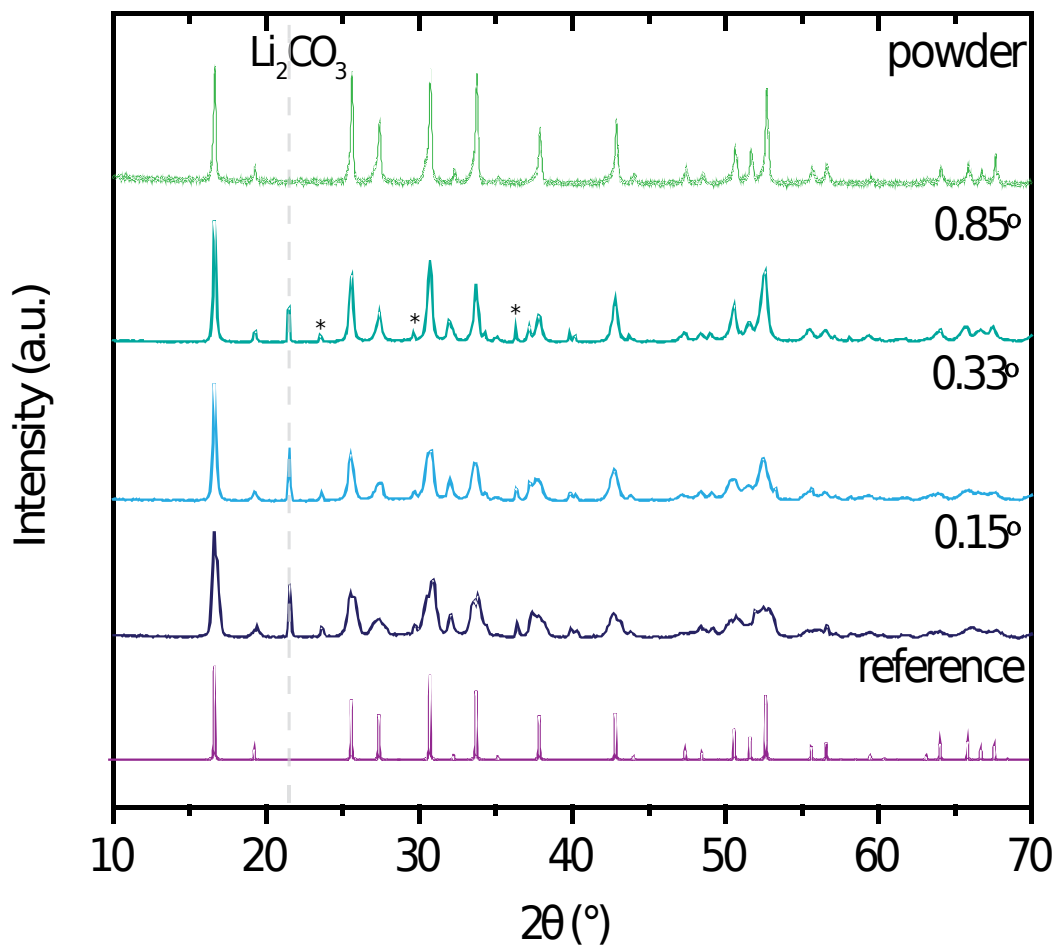

Figure 2. Low resolution GIXRD spectra collected at grazing angles of 0.15º, 0.33º and 0.85º. A LLZO powder diffraction pattern (top) and a calculated reference from reference [32] is also provided (bottom). * indicates minor impurity phases including $LiAlO_2$ and $LaAlO_3$.

We used both high resolution GIXRD and GI-EXAFS to confirm our speculation that the lattice close to the surface of the pellet shrank due to air exposure. Two characteristic reflections of the garnet structure were scanned, namely the peaks at approximately $2\theta=$ 16.7º and 25.8º, corresponding to the (211) and (321) lattice planes. These reflections were fine scanned at various incident angles going from shallow to deeper into the bulk (Figure 3). The trends in both sets of data are consistent in that peak positions gradually shift to lower 2θ values at deeper angles. For example, for the (321) peak, at an incident angle of 0.33º, the position was 25.72º, which shifted to ~25.64º at an incident angle of 2º (depth of ~ 0.32 µm). This means that the d-spacings for the 211 and 311 crystallographic planes are slightly smaller at the surface than in the bulk. Based on Bragg's law, $2d\sin\theta=n\lambda$ (n=1, λ=1.54 Å), we estimated that for the 321 planes, the d spacings at the surface and in the bulk are 3.449 Å and 3.462 Å, respectively. Likewise, the d spacings for the 211 planes at the surface and in the bulk were calculated to be 5.271 Å and 5.296 Å. It is also interesting that the peak shift was gradual, implying a gradient in the d-spacing from the bulk to surface.
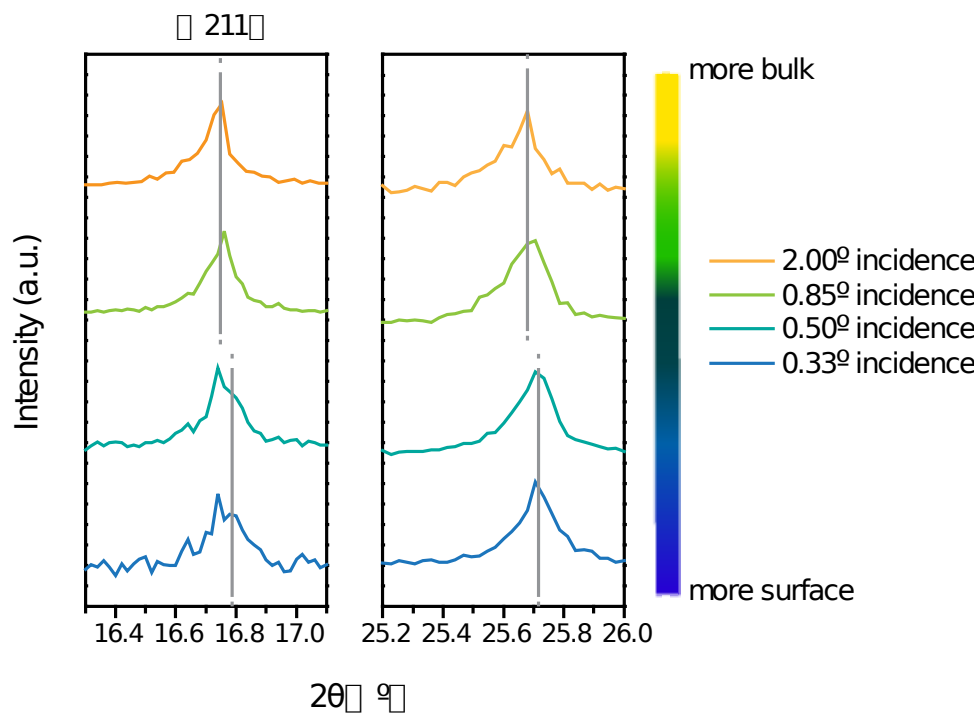
Figure 3. High Resolution GIXRD of LLZO characteristic (211) and (321) peaks at varying incident angles, from bottom to top.

Figure 4 represents transformed Zr K-edge GI-XAS data. At the Zr-K edge energy (~18 keV photon energy), the X-ray penetration depths at 0.15º and 3 º incident angles were estimated to be 35 nm and 2.4 μm. Because the GI-XAS data was collected using a fluorescence detector, there are some self-absorption effects in these measurements. However, bond distances and absorption edges can usually be measured accurately.[33] For comparison, we also performed Zr-K edge EXAFS using a mixture of dilute LLZO powder (from a crushed pellet) and sucrose at SSRL beamline 4-1 in transmission mode, which eliminates the self-absorption effect). In Figure 4 (a), the uncorrected radial distribution plot of the LLZO powder showed a clear two shell

15

structure; the nearest neighbor corresponding to the Zr-O atomic distance is 1.503 Å, while the second shell is at approximately 3.0 Å, corresponding to the Zr-La atomic distance. Note the phase is not corrected in the EXAFS data due to lack of reference data, thus the calculated atomic distances are shorter than the theoretical values. In the GI-XAS measurements, at a 3º incident angle (an estimated probing depth of 2.4 μm, corresponding to the bulk), the Zr-O and Zr-La atomic distances are nearly identical to that of the powder. However, the data taken at the 0.15º incident angle shows smaller distances for both the Zr-O atomic distance (1.411Å) and for the Zr-La atomic distance, which shrank to 2.86 Å. Note that the penetration depth of the GI-XAS experiment was much deeper at high angles compared to that of the GI-XRD due to the X-ray photon energy.
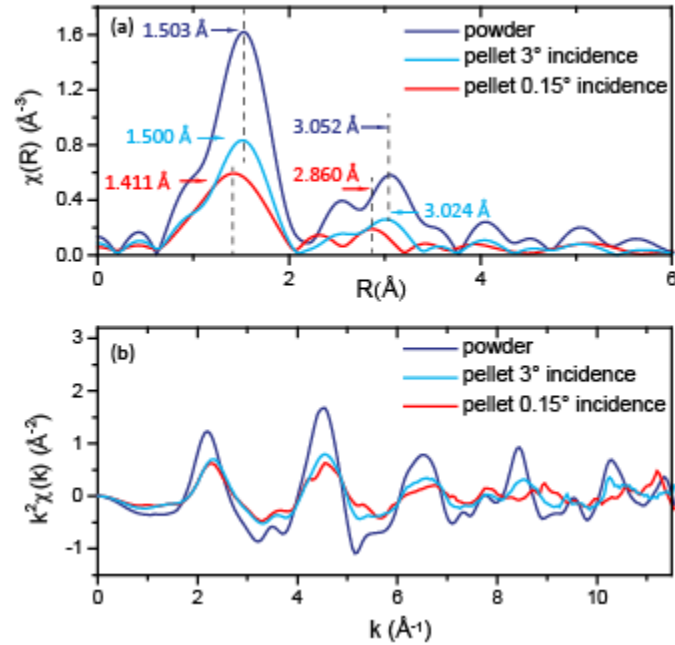
Figure 4. (a) Fourier transform Zr K edge EXAFS spectra (phase uncorrected). (b) Zr K edge EXAFS oscillation.

A consideration of the GI-XRD and GI-XAS experiments shows consistent results; that changes occur to LLZO surfaces exposed to moisture/air in the form of lattice shrinkage and lattice strain. There is a gradient going from the very top surface into the bulk; the sub-surface LLZO lattice shrank less compared to the top surface and the bulk was not affected. In Al substituted LLZO, the lattice parameter is positively related to lithium content and inversely related to Al content, which substitutes at Li sites.[14] Similarly, in the exposed LLZO where formation of LiOH and Li_2CO_3 removes the lattice lithium, proton replacement of Li^+ led to lattice shrinkage in the protonated LLZO. [34-36] Given that the chemical reaction involves interaction between a gas or liquid and a solid, a gradient of protons and lithium ions can be established where a high concentration of protons and a low concentration of Li^+ causes more lattice shrinkage at the top surface, while deeper into the sample a lower concentration of protons leads to less lattice shrinkage.

Considering the correlation between protonation and lattice parameter, we speculate that proton and lithium content might serve as useful indicators of the relative shrinkage in the local crystal structure and vice versa. In order to establish this semi-quantitative correlation, we used *ab*

17

initio molecular dynamics simulations to establish the relative lattice shrinkage as a function of proton/lithium content in the lattice at 300K. For the simplicity of the simulation, we used an Al free cubic LLZO structure for the simulations and H atoms were intentionally added to replace Li atoms in the garnet crystal lattice for the following compositions: $Li_{56}La_{24}Zr_{16}O_{96}$, $Li_{52}H_4La_{24}Zr_{16}O_{96}$ and $Li_{49}H_7La_{24}Zr_{16}O_{96}$. The DFT-MD method was used to extrapolate the median values of the Zr-O and Zr-La atomic distances. Both were found to decrease with increasing proton content (lower Li content).
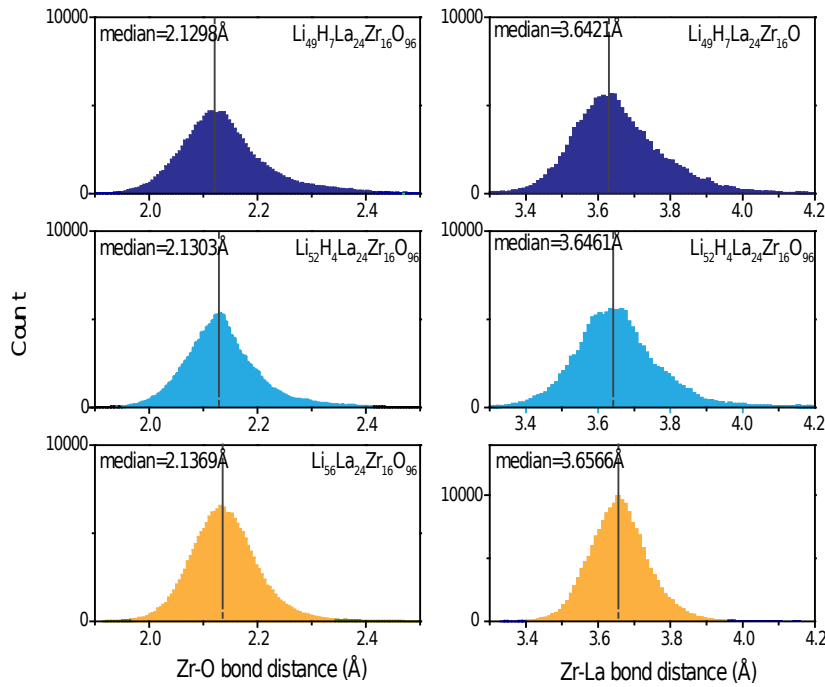
Figure 5. Histogram of Zr-O and Zr-La atomic distances from ab initio MD simulations using compositions of $Li_{56}La_{24}Zr_{16}O_{96}$ (bottom), $Li_{52}H_4La_{24}Zr_{16}O_{96}$ (middle), and $Li_{49}H_7La_{24}Zr_{16}O_{96}$ (top). Median values of Zr-O atomic distances are provided.

By careful investigation of the surface of the LLZO exposed to air for one week, we found evidence of a gradient in the lattice parameter going from the surface into the bulk due to proton exchange. This is correlated with formation of a Li_2CO_3 layer on the very top surface. Annealing at temperature higher than 500ºC has been shown to be effective at removing the surface LiOH and Li_2CO_3 species.[18] However, we speculated that heating at lower temperatures in an inert atmosphere could possibly reverse this process as well. To investigate this, we utilized APXPS under an inert argon (Ar) atmosphere to study the surface chemistry evolution during heating to 250ºC. (Note the pressure that could be achieved in the XPS chamber was 200 mTorr, which is lower than typically available in a glovebox environment). The previously air-exposed sample surface appeared to be fully covered by Li_2CO_3 because neither a Zr nor a La signal could be detected at 25°C, and carbonate carbon, carbonate oxygen and Li belonging to Li_2CO_3 were observed in the C1s, O1s and Li1s region, as shown in Figure 6. Based on this observation, the thickness of Li_2CO_3 is greater than that of the probing depth (2-3 nm) of the surface sensitive XPS technique. Note it is possible that some amount of LiOH may co-exist with Li_2CO_3. Typical values of the surface Li_2CO_3 thickness have been estimated to be between 3-100 nm after several days of ambient air exposure. [13] When the specimen was slowly heated up to 250º C (at a rate of ~3-5 °C/min), the $C(CO_3)$ peak at 290 eV almost completely disappeared. The adventitious peak belonging to (C-C) at (284.8 eV) became sharper, probably because some surface absorbed

carbon species were desorbed under these conditions. In the O 1s region, a second oxygen peak (528 eV) evolved after the sample was heated in the XPS chamber, which can be assigned to the garnet lattice oxygen. Similarly, a Zr *3d* doublet emerged, which can be assigned to lattice Zr. We also observed a small shoulder peak in the Li *1s* region, where we speculate could be Li_2O due to LiOH decomposition. These results indicate that Li_2CO_3 was removed from the surface by the heating process. We collected APXPS spectra at different temperatures between ambient to 250ºC over a period of about 6 hours, to analyses the relative ratio of $C(CO_3)$/C-C and $O(lattice)/O(CO_3)$, shown in Figure 7. Below 150ºC, the ratio remained relatively constant with a slight increase for the $C(CO_3)$/C-C ratio between 25 ºC to 80 ºC, which is attributable to desorption of the absorbed hydro-carbon species. A sharp jump in both $C(CO_3)$/C-C and $O(lattice)/O(CO_3)$ ratios were found at temperatures > 150 ºC, indicating that the onset temperature of the decomposition reaction of the surface Li_2CO_3 was close to 150 ºC. Due to the dynamic nature of the XPS experiment (data collection was slower than the temperature ramp rate), there is some uncertainty in determining the exact onset temperature. However, it is clear that the estimated onset temperature of the decomposition reaction is much lower than that of simple decomposition of Li_2CO_3 to CO_2 (reaction 1), which has been reported to be between 620 -1000 ºC (melting of Li_2CO_3 occurs at ~720 ºC, according to DSC measurements).[37,38]

$$(1) Li_2CO_3(s) = Li_2O(s) + CO_2(g)$$
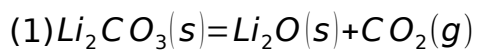
It is likely, therefore, that the surface chemical reaction involved the protonated LLZO surface, with a reversal of the proton exchange reaction occurring concurrent with the decomposition of Li_2CO_3.
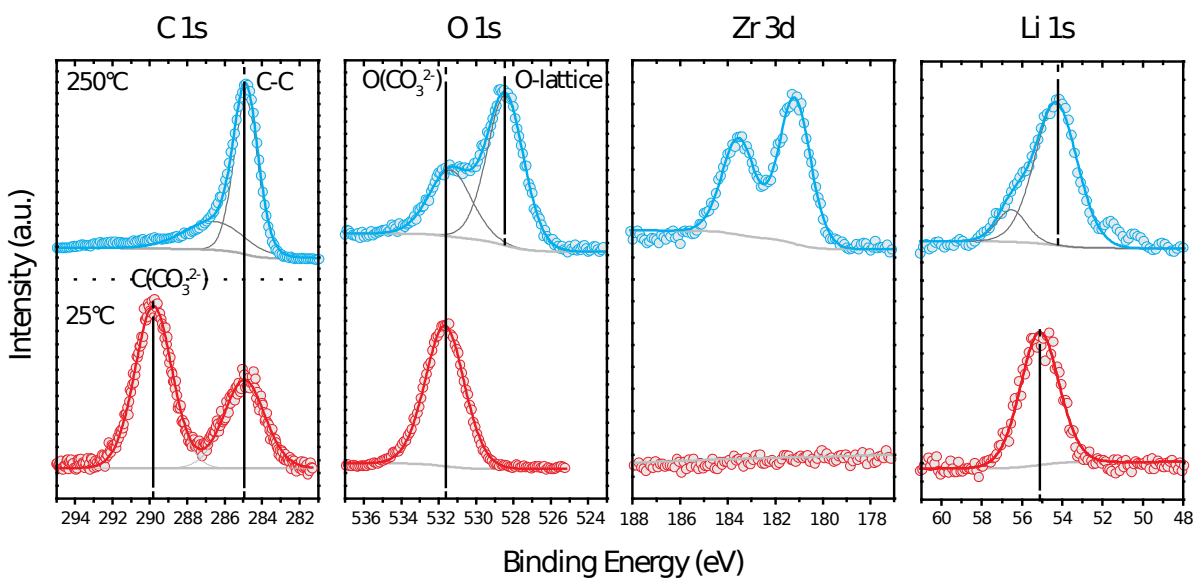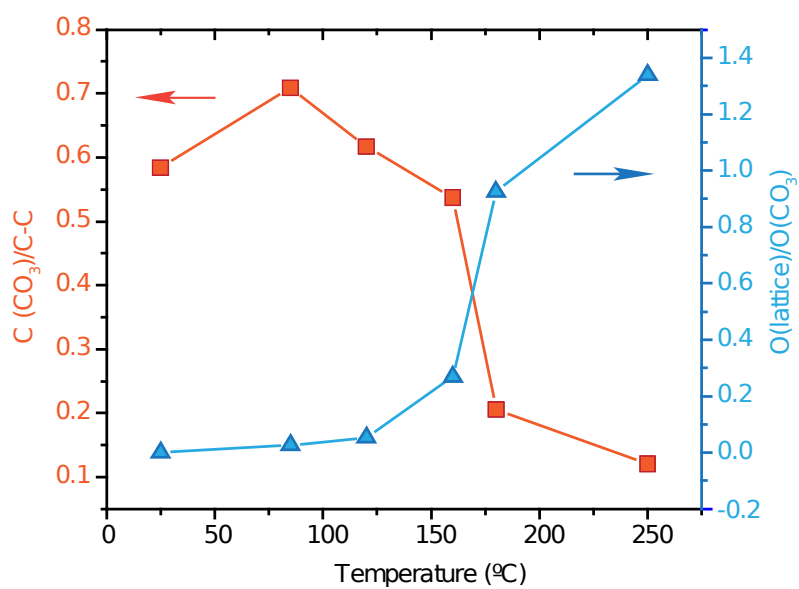
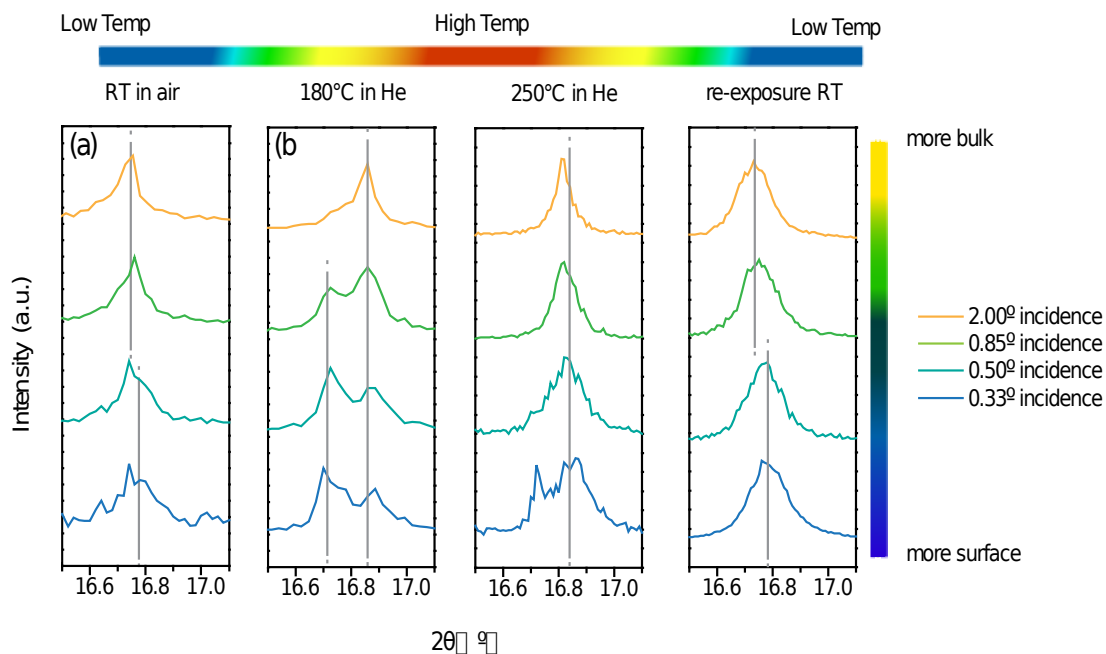Figure 7. Ratios of C(CO$_3$)/C-C and O(lattice)/O(CO$_3$) at different temperatures

derived from APXPS data.

Figure 8. *In-situ* high resolution GIXRD spectra of LLZO pellet after exposure (a) at ambient room temperature; (b) heated in He at 180ºC; (c) heated in He at 250ºC and (d) re-exposed to air/moisture for a month.

We used high resolution GIXRD to further investigate the crystal structure evolution when heated *in-situ* under helium. He gas was selected because its X-ray absorption is lower than that of Ar. As already discussed above, we observed a gradual shifting of the 211 peak position as a function of probing depth for the air-exposed sample, indicating a gradient in the lattice parameter. Upon heating, there is a dramatic change in the region

where the 211 peak appears. For the sample heated at 180ºC under He and measured at a 2º incident angle, corresponding to a depth of 0.32 µm, a single 211 peak at ~16.85º is observed, close to the value found at room temperature. At an incident angle of 0.85º with a shallower probing depth of 120 nm, a second peak appears at 2θ =16.7 º. At even smaller angles of 0.5º (depth of ~62 nm) and 0.33º (depth of ~20 nm), two diffraction peaks are still evident but the relative intensity of the lower angle peak increased while the other one decreased. At the very surface, (incident angle of 0.15º, or 3 nm) only the 16.7º peak is apparent in the diffraction pattern. Orera et al. suggested that, upon exposure to moisture, a hydrated cubic LLZO phase formed that belongs to the space group $I\acute{4}3d$.[39] When this specimen was further heated at temperature above 300ºC, it formed a regular LLZO cubic phase belonging to space group $Ia\acute{3}d$. Wagner et al. also showed that in Ga and Fe substituted garnets, the crystal structure is dependent on the Ga substitution level. The structure belonging to the $Ia\acute{3}d$ space group contains a higher lithium content (and lower substitution content) and has a slightly larger lattice parameter compared to the one (with higher substitution and low Li content) belonging to the $I\acute{4}3d$ space group. [40-43] This is consistent with what we observed in our case. Upon exposure to moisture, proton exchange induced a structural change on the LLZO surface to a phase with a hydrated $I\acute{4}3d$ symmetry. Upon heating, after the Li_2CO_3 reacts back with the surface, Li is reintroduced into the structure and it converts back into the

phase belonging to the $Ia\bar{3}d$ space group with the larger lattice parameter. The reaction at the sub surface is slower to occur, and the $I\bar{4}3d$ phase with a smaller lattice parameter predominates. When the specimen was further heated to 250ºC, it drove the reaction further to homogenize the lithium content on the surface and in the sub-surface, as shown in Figure 8(c). There, the two peaks due to the co-existence of the $I\bar{4}3d$ and $Ia\bar{3}d$ phases appear at the shallowest probing depths but not deeper into the sample. After the *in-situ* measurement, the specimen was re-exposed to air for one month. The lattice parameter gradient was re-established (as shown in Figure 8(d)), similar to that seen in Figure 8(a). It should be noted here that some researchers have reported lattice expansion when garnet powders or pellets are soaked in liquid water, without a change in space group. [44] The difference in behavior is probably related to compositional differences (reference 44 concerns a Ta-substituted LLZO) including Li stoichiometry. [45]

We assembled a Li/LLZO/Li symmetric cell to evaluate the effect of sample heating on the interfacial impedance. Air-exposed LLZO has Li_2CO_3 on the surface, which results in high contact resistance at the Li metal electrode; our previous studies indicate that removal of the Li_2CO_3 by polishing greatly reduced the interfacial impedance.[13,20,46] In the Nyquist plots, two semicircles were observed. The semicircle at high frequency was attributed to the total resistance of the LLZO pellet and the lower frequency semicircle was attributed to the sum of two Li/LLZO interfacial resistances.

Impedance was determined by fitting (RQ)(RQ) equivalent circuit in the previous papers.[13] The cell in this study containing an air-exposed sample showed a total interfacial impedance of 1.9 MΩ before treatment. When the sample was subsequently heated to 250 ºC in an Ar-filled glovebox and cooled down to 25 ºC for electrical measurements, the total interfacial impedance (containing two Li/garnet interfaces on both sides of a pellet) was greatly reduced to 2547 Ω and then to 750 Ω after heating to 250ºC for 1 hours and to 250ºC overnight for 12 hours, respectively (See Figure 9). This greatly reduced total interfacial impedance corresponds to a normalized area specific resistance (ASR) of 607 $\Omega \cdot cm^2$ and 178 $\Omega \cdot cm^2$, using an effective contact area of 0.477 cm^2 based on the size of the pellet. This value is similar to what was reported in the literature for a sample with similar grain sizes.[13,47] The similarity of the results to ones we obtained previously from polished samples suggests that the heat treatment was effective at removing Li_2CO_3. These results suggest that a low resistance interface with LLZO solid electrolyte can be achieved without stringent moisture and CO_2 control, since the pristine state can be recovered by a low temperature treatment even after the device is assembled and packed. This simplifies the manufacturing and integration process.
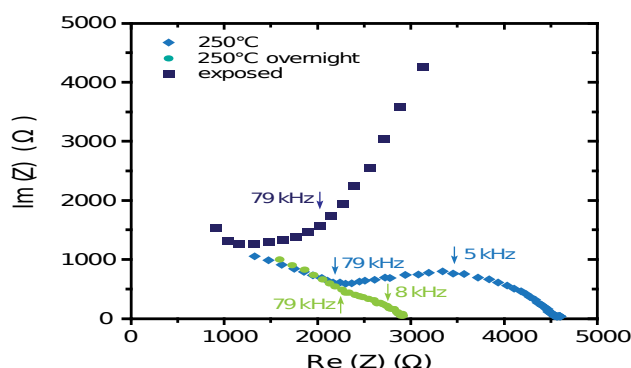
Figure 9. Nyquist plot of impedance data obtained on Li/LLZO/Li symmetrical cells, where the LLZO has been exposed to air (black squares), treated at 250°C for 1 hour (blue diamonds), or treated at 250°C overnight for 12 h (green circles).

Lastly, we consider that for LLZO powders, similar phenomena may occur extensively due to the relatively larger surface area, compared to pellets. The bright-field scanning transmission electron microscopy (STEM) image recorded in a cold-field aberration-corrected dedicated STEM (Fig. 10) suggests that the crystalline LLZO particle surface developed a 4-5 nm thick layer after air exposure, which can be attributed to carbonate formation associated with proton exchange in LLZO. An electron energy loss spectrum

confirmed that this layer is lithium carbonate (not shown). This thickness agrees with the previous XPS analysis. Upon sintering, depending on the heating rate, surface Li_2CO_3 most likely reacts back with the LLZO lattice given enough time. The surface Li_2CO_3 melts at ~650ºC (well below the temperature at which LLZO is densified) and participates in the sintering process, which results in the large grain size observed in these pellets.
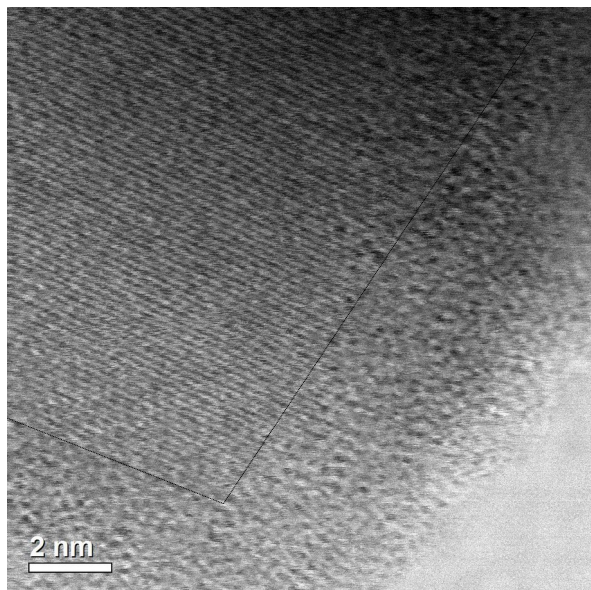

Figure 10. Bright-field scanning transmission electron microscopy image of air-exposed LLZO particle.

Conclusions and Summary

Several depth-profiling techniques were used to characterize the surfaces of Al-substituted LLZO pellets exposed to air. These experiments revealed that a structural and chemical gradient exists, consistent with

proton exchange of the LLZO, which extends from the surface into the sub-surface. Li_2CO_3 also forms on the top surface, concomitant with this process. Degraded samples were monitored as they were heated under inert atmosphere, using *in-situ* AP-XPS and GI-XRD. During the heating process, the Li_2CO_3 reacts back with the LLZO and the proton exchange is reversed to re-form the original structure, with the top surface more readily undergoing these changes than the sub-surface. Raising the temperature from 180°C to 250°C accelerated the reaction below the surface. Re-exposure to air induces the proton exchange reaction again, indicating that the process is highly reversible. This observation is significant because it implies that a simple treatment at relatively low temperatures is effective for reversing LLZO degradation. Advanced protection layer or interfacial coating may not be necessary to achieve good interfacial properties. Impedance experiments on symmetrical cells containing air-exposed LLZO and samples treated at 250°C for differing lengths of time confirm this; the area-specific impedance of symmetrical cells containing heat-treated LLZO was greatly reduced compared to one containing air-exposed LLZO and approached that of cells containing pristine LLZO in which the Li_2CO_3 was removed by mechanical polishing.

References

(1)   Goodenough, J. B.; Kim, Y. Challenges for Rechargeable Li Batteries [†]. *Chem. Mater.* **2010**, *22* (3), 587–603. https://doi.org/10.1021/cm901452z.

(2)   Janek, J.; Zeier, W. G. A Solid Future for Battery Development. *Nat. Energy* **2016**, *1* (9), 1–4. https://doi.org/10.1038/nenergy.2016.141.

(3)   Zhang, Z.; Shao, Y.; Lotsch, B.; Hu, Y. S.; Li, H.; Janek, J.; Nazar, L. F.; Nan, C. W.; Maier, J.; Armand, M.; et al. New Horizons for Inorganic Solid State Ion Conductors. *Energy Environ. Sci.* **2018**, *11* (8), 1945–1976. https://doi.org/10.1039/c8ee01053f.

(4)   Richards, W. D.; Miara, L. J.; Wang, Y.; Kim, J. C.; Ceder, G. Interface Stability in Solid-State Batteries. *Chem. Mater.* **2016**, *28* (1), 266–273. https://doi.org/10.1021/acs.chemmater.5b04082.

(5)   Zhu, Y.; He, X.; Mo, Y. Origin of Outstanding Stability in the Lithium Solid Electrolyte Materials: Insights from Thermodynamic Analyses Based on First-Principles Calculations. *ACS Appl. Mater. Interfaces*

2015, *7* (42), 23685–23693. https://doi.org/10.1021/acsami.5b07517.

(6)   Zhu, Y.; He, X.; Mo, Y. First Principles Study on Electrochemical and Chemical Stability of Solid Electrolyte–electrode Interfaces in All-Solid-State Li-Ion Batteries. *J. Mater. Chem. A* **2016**, *4* (9), 3253–3266. https://doi.org/10.1039/C5TA08574H.

(7)   Lin, F.; Liu, Y.; Yu, X.; Cheng, L.; Singer, A.; Shpyrko, O. G.; Xin, H. L.; Tamura, N.; Tian, C.; Weng, T.-C.; et al. Synchrotron X-Ray Analytical Techniques for Studying Materials Electrochemistry in Rechargeable Batteries. *Chem. Rev.* **2017**, *117* (21), 13123–13186. https://doi.org/10.1021/acs.chemrev.7b00007.

(8)   Hartmann, P.; Leichtweiss, T.; Busche, M. R.; Schneider, M.; Reich, M.; Sann, J.; Adelhelm, P.; Janek, J. Degradation of NASICON-Type Materials in Contact with Lithium Metal: Formation of Mixed Conducting Interphases (MCI) on Solid Electrolytes. *J. Phys. Chem. C* **2013**, *117* (41), 21064–21074. https://doi.org/10.1021/jp4051275.

(9)   Yamada, H.; Takemoto, K. Local Structure and Composition Change at Surface of Lithium-Ion Conducting Solid Electrolyte. *Solid State Ionics* **2016**, *285*, 41–46. https://doi.org/10.1016/j.ssi.2015.08.019.

(10)   Murugan, R.; Thangadurai, V.; Weppner, W. Fast Lithium Ion Conduction in Garnet-Type Li7La3Zr2O12. *Angew. Chemie - Int. Ed.* **2007**, *46* (41), 7778–7781. https://doi.org/10.1002/anie.200701144.

(11) Thangadurai, V.; Pinzaru, D.; Narayanan, S.; Baral, A. K. Fast Solid-State Li Ion Conducting Garnet-Type Structure Metal Oxides for Energy Storage. *J. Phys. Chem. Lett.* **2015**, *6* (2), 292–299. https://doi.org/10.1021/jz501828v.

(12) Thangadurai, V.; Narayanan, S.; Pinzaru, D. Garnet-Type Solid-State Fast Li Ion Conductors for Li Batteries: Critical Review. *Chem. Soc. Rev.* **2014**, *43* (13), 4714–4727. https://doi.org/10.1039/c4cs00020j.

(13) Cheng, L.; Crumlin, E. J.; Chen, W.; Qiao, R.; Hou, H.; Franz Lux, S.; Zorba, V.; Russo, R.; Kostecki, R.; Liu, Z.; et al. The Origin of High Electrolyte-Electrode Interfacial Resistances in Lithium Cells Containing Garnet Type Solid Electrolytes. *Phys. Chem. Chem. Phys.* **2014**, *16* (34), 18294–18300. https://doi.org/10.1039/c4cp02921f.

(14) Cheng, L.; Park, J. S.; Hou, H.; Zorba, V.; Chen, G.; Richardson, T.; Cabana, J.; Russo, R.; Doeff, M. Effect of Microstructure and Surface Impurity Segregation on the Electrical and Electrochemical Properties of Dense Al-Substituted Li 7 La 3 Zr 2 O 12. *J. Mater. Chem. A* **2014**, *2* (1), 172–181. https://doi.org/10.1039/C3TA13999A.

(15) Orera, A.; Larraz, G.; Rodríguez-Velamazán, J. A.; Campo, J.; Sanjuán, M. L. Influence of Li + and H + Distribution on the Crystal Structure of Li 7– x H x La 3 Zr 2 O 12 (0 ≤ x ≤ 5) Garnets. *Inorg. Chem.* **2016**, *55* (3), 1324–1332. https://doi.org/10.1021/acs.inorgchem.5b02708.

(16) Larraz, G.; Orera, A.; Sanjuán, M. L.; Sanjuan, M. L. Cubic Phases of Garnet-Type Li7La3Zr2O12: The Role of Hydration. *J. Mater. Chem. A* **2013**, *1* (37), 11419–11428. https://doi.org/10.1039/C3TA11996C.

(17) Cheng, L.; Iyer, S.; Gardener, W.; Holme, T.; Li, S.; Chao, C.; Donnelly, N.; Allenic, A. Annealed Garnet Electrolyte Separators. U.S. Patent 9966630 B2, 2018.

(18) Sharafi, A.; Kazyak, E.; Davis, A. L.; Yu, S.; Thompson, T.; Siegel, D. J.; Dasgupta, N. P.; Sakamoto, J. Surface Chemistry Mechanism of Ultra-Low Interfacial Resistance in the Solid-State Electrolyte Li 7 La 3 Zr 2 O 12. *Chem. Mater.* **2017**, *29* (18), 7961–7968. https://doi.org/10.1021/acs.chemmater.7b03002.

(19) Sharafi, A.; Yu, S.; Naguib, M.; Lee, M.; Ma, C.; Meyer, H. M.; Nanda, J.; Chi, M.; Siegel, D. J.; Sakamoto, J. Impact of Air Exposure and Surface Chemistry on Li–Li 7 La 3 Zr 2 O 12 Interfacial Resistance. *J. Mater. Chem. A* **2017**, *5* (26), 13475–13487. https://doi.org/10.1039/C7TA03162A.

(20) Cheng, L.; Wu, C. H.; Jarry, A.; Chen, W.; Ye, Y.; Zhu, J.; Kostecki, R.; Persson, K.; Guo, J.; Salmeron, M.; et al. Interrelationships among Grain Size, Surface Composition, Air Stability, and Interfacial Resistance of Al-Substituted Li 7 La 3 Zr 2 O 12 Solid Electrolytes. *ACS Appl. Mater. Interfaces* **2015**, *7* (32), 17649–17655. https://doi.org/10.1021/acsami.5b02528.

(21) Duan, H.; Zheng, H.; Zhou, Y.; Xu, B.; Liu, H. Stability of Garnet-Type Li Ion Conductors: An Overview. *Solid State Ionics* **2018**, *318*, 45–53. https://doi.org/10.1016/J.SSI.2017.09.018.

(22) Xia, W.; Xu, B.; Duan, H.; Guo, Y.; Kang, H.; Li, H.; Liu, H. Ionic Conductivity and Air Stability of Al-Doped $Li_7La_3Zr_2O_{12}$ Sintered in Alumina and Pt Crucibles. *ACS Appl. Mater. Interfaces* **2016**, *8* (8), 5335–5342. https://doi.org/10.1021/acsami.5b12186.

(23) Brugge, R. H.; Hekselman, A. K. O.; Cavallaro, A.; Pesci, F. M.; Chater, R. J.; Kilner, J. A.; Aguadero, A. Garnet Electrolytes for Solid State Batteries: Visualization of Moisture-Induced Chemical Degradation and Revealing Its Impact on the Li-Ion Dynamics. *Chem. Mater.* **2018**, *30* (11), 3704–3713. https://doi.org/10.1021/acs.chemmater.8b00486.

(24) Hofstetter, K.; Samson, A. J.; Narayanan, S.; Thangadurai, V. Present Understanding of the Stability of Li-Stuffed Garnets with Moisture, Carbon Dioxide, and Metallic Lithium. *J. Power Sources* **2018**, *390*, 297–312. https://doi.org/10.1016/J.JPOWSOUR.2018.04.016.

(25) Ravel, B.; Newville, M.; IUCr. *ATHENA* , *ARTEMIS* , *HEPHAESTUS* : Data Analysis for X-Ray Absorption Spectroscopy Using *IFEFFIT*. *J. Synchrotron Radiat.* **2005**, *12* (4), 537–541. https://doi.org/10.1107/S0909049505012719.

(26) Grass, M. E.; Karlsson, P. G.; Aksoy, F.; Lundqvist, M.; Wannberg, B.;

Mun, B. S.; Hussain, Z.; Liu, Z. New Ambient Pressure Photoemission Endstation at Advanced Light Source Beamline 9.3.2. *Rev. Sci. Instrum.* **2010**, *81* (5), 053106. https://doi.org/10.1063/1.3427218.

(27) Ong, S. P.; Richards, W. D.; Jain, A.; Hautier, G.; Kocher, M.; Cholia, S.; Gunter, D.; Chevrier, V. L.; Persson, K. a.; Ceder, G. Python Materials Genomics (Pymatgen): A Robust, Open-Source Python Library for Materials Analysis. *Comput. Mater. Sci.* **2013**, *68*, 314–319. https://doi.org/10.1016/j.commatsci.2012.10.028.

(28) Kresse, G. Efficient Iterative Schemes for Ab Initio Total-Energy Calculations Using a Plane-Wave Basis Set. *Physical Review B*. 1996, pp 11169–11186. https://doi.org/10.1103/PhysRevB.54.11169.

(29) Kresse, G.; Joubert, D. From Ultrasoft Pseudopotentials to the Projector Augmented-Wave Method. *Phys. Rev. B* **1999**, *59* (3), 1758–1775.

(30) Perdew, J. P.; Burke, K.; Ernzerhof, M. Generalized Gradient Approximation Made Simple. *Phys. Rev. Lett.* **1996**, *77* (18), 3865–3868.

(31) Jain, A.; Hautier, G.; Moore, C. J.; Ping Ong, S.; Fischer, C. C.; Mueller, T.; Persson, K. A.; Ceder, G. A High-Throughput Infrastructure for Density Functional Theory Calculations. *Comput. Mater. Sci.* **2011**, *50* (8), 2295–2310. https://doi.org/10.1016/J.COMMATSCI.2011.02.023.

(32) Geiger, C. A.; Alekseev, E.; Lazic, B.; Fisch, M.; Armbruster, T.; Langner,

R.; Fechtelkord, M.; Kim, N.; Pettke, T.; Weppner, W. Crystal Chemistry and Stability of "Li 7 La 3 Zr 2 O 12 " Garnet: A Fast Lithium-Ion Conductor. *Inorg. Chem.* **2011**, *50* (3), 1089–1097. https://doi.org/10.1021/ic101914e.

(33) Tröger, L.; Arvanitis, D.; Baberschke, K.; Michaelis, H.; Grimm, U.; Zschech, E. Full Correction of the Self-Absorption in Soft-Fluorescence Extended x-Ray-Absorption Fine Structure. *Phys. Rev. B* **1992**, *46* (6), 3283–3289. https://doi.org/10.1103/PhysRevB.46.3283.

(34) Truong, L.; Thangadurai, V. First Total H + /Li + Ion Exchange in Garnet-Type Li 5 La 3 Nb 2 O 12 Using Organic Acids and Studies on the Effect of Li Stuffing. *Inorg. Chem.* **2012**, *51* (3), 1222–1224. https://doi.org/10.1021/ic202491m.

(35) Larraz, G.; Orera, A.; Sanz, J.; Sobrados, I.; Diez-Gómez, V.; Sanjuán, M. L. NMR Study of Li Distribution in Li7-x HxLa3Zr2O12 Garnets. *J. Mater. Chem. A* **2015**, *3* (10), 5683–5691. https://doi.org/10.1039/C4TA04570J.

(36) Larraz, G.; Orera, A.; Sanjuán, M. L. Cubic Phases of Garnet-Type Li7La3Zr2O12: The Role of Hydration. *J. Mater. Chem. A* **2013**, *1* (37), 11419. https://doi.org/10.1039/c3ta11996c.

(37) Ren, Y.; Deng, H.; Chen, R.; Shen, Y.; Lin, Y.; Nan, C.-W. Effects of Li Source on Microstructure and Ionic Conductivity of Al-Contained Li6.75La3Zr1.75Ta0.25O12 Ceramics. *J. Eur. Ceram. Soc.* **2015**, *35* (2),

561–572. https://doi.org/10.1016/j.jeurceramsoc.2014.09.007.

(38) Timoshevskii, A. N.; Ktalkherman, M. G.; Emel'kin, V. A.; Pozdnyakov, B. A.; Zamyatin, A. P. High-Temperature Decomposition of Lithium Carbonate at Atmospheric Pressure. *High Temp.* **2008**, *46* (3), 414–421. https://doi.org/10.1134/S0018151X0803019X.

(39) Orera, A.; Larraz, G.; Rodríguez-Velamazán, J. A.; Campo, J.; Sanjuán, M. L. Influence of Li^+ and H^+ Distribution on the Crystal Structure of $Li_{7-x}H_xLa_3Zr_2O_{12}$ ($0 \leq x \leq 5$) Garnets. *Inorg. Chem.* **2016**, *55* (3), 1324–1332. https://doi.org/10.1021/acs.inorgchem.5b02708.

(40) Wagner, R.; Redhammer, G. J.; Rettenwander, D.; Senyshyn, A.; Schmidt, W.; Wilkening, M.; Amthauer, G. Crystal Structure of Garnet-Related Li-Ion Conductor $Li_{7-3x}Ga_xLa_3Zr_2O_{12}$: Fast Li-Ion Conduction Caused by a Different Cubic Modification? *Chem. Mater.* **2016**, *28* (6), 1861–1871. https://doi.org/10.1021/acs.chemmater.6b00038.

(41) Rettenwander, D.; Wagner, R.; Reyer, A.; Bonta, M.; Cheng, L.; Doeff, M. M.; Limbeck, A.; Wilkening, M.; Amthauer, G. Interface Instability of Fe-Stabilized $Li_7La_3Zr_2O_{12}$ versus Li Metal. *J. Phys. Chem. C* **2018**, *122* (7), 3780–3785. https://doi.org/10.1021/acs.jpcc.7b12387.

(42) Wagner, R.; Redhammer, G. J.; Rettenwander, D.; Tippelt, G.; Welzl, A.; Taibl, S.; Fleig, J.; Franz, A.; Lottermoser, W.; Amthauer, G. Fast Li-Ion-

Conducting Garnet-Related Li $_{7-3x}$ Fe $_x$ La $_3$ Zr $_2$ O $_{12}$ with Uncommon I $\bar{4}3d$ Structure. *Chem. Mater.* **2016**, *28* (16), 5943–5951. https://doi.org/10.1021/acs.chemmater.6b02516.

(43)   Rettenwander, D.; Redhammer, G.; Preishuber-Pflügl, F.; Cheng, L.; Miara, L.; Wagner, R.; Welzl, A.; Suard, E.; Doeff, M. M.; Wilkening, M.; et al. Structural and Electrochemical Consequences of Al and Ga Cosubstitution in Li $_7$ La $_3$ Zr $_2$ O $_{12}$ Solid Electrolytes. *Chem. Mater.* **2016**, *28* (7), 2384–2392.

https://doi.org/10.1021/acs.chemmater.6b00579.

(44)   Yow, Z. F.; Oh, Y. L.; Gu, W.; Rao, R. P.; Adams, S. Effect of Li+/H+ Exchange in Water Treated Ta-Doped Li7La3Zr2O12. *Solid State Ionics* **2016**, *292*, 122–129. https://doi.org/10.1016/J.SSI.2016.05.016.

(45)   Galven, C.; Fourquet, J. L.; Crosnier-Lopez, M. P.; Le Berre, F. Instability of the Lithium Garnet Li7La3Sn 2O12: Li+/H+ Exchange and Structural Study. *Chem. Mater.* **2011**, *23* (7), 1892–1900. https://doi.org/10.1021/cm103595x.

(46)   Cheng, L.; Chen, W.; Kunz, M.; Persson, K. A.; Tamura, N.; Chen, G.; Doeff, M. M. Effect of Surface Microstructure on Electrochemical Performance of Garnet Solid Electrolytes. *ACS Appl. Mater. Interfaces* **2015**, *7* (3), 2073–2081. https://doi.org/10.1021/am508111r.

(47)   Cheng, L.; Hou, H.; Lux, S.; Kostecki, R.; Davis, R.; Zorba, V.; Mehta, A.;

Doeff, M. Enhanced Lithium Ion Transport in Garnet-Type Solid State

Electrolytes. *J. Electroceramics* **2017**, *38* (2–4), 168–175.

https://doi.org/10.1007/s10832-017-0080-3.

TOC Graphic

surface Li$_2$CO$_3$

Li depleted surface

degraded LLZO

Recovery of LLZO removes surface Li$_2$CO$_3$ and rejuvenates Li distribution

C 1s

O 1s

250°C

C-C

O(CO$_3^{2-}$)

O-lattice

25°C

C(CO$_3^{2-}$)

Intensity (a.u.)

294 290 286 282

536 532 528 524

Binding Energy (eV)

clean LLZO surface

Li content recovered

recovered LLZO

Air exposure leads to LLZO degradation depleting surface Li